universe

MDPI

Article

Probing ALP-Photon Oscillations with Fermi-LAT Observation of the Andromeda Galaxy

Jun Li

School of Physical Science and Technology, Xinjiang University, Urumqi 830017, China; mjli@xju.edu.cn

Abstract

Axion-like particles (ALPs) can induce energy-dependent irregularities in gamma-ray spectra through ALP-photon oscillation in astrophysical magnetic fields. In this study, we investigate the impact of this effect on the γ-ray emission from the Andromeda Galaxy (M31). We employ the CL_s method to set constraints on the ALP parameters. We find that ALP-photon oscillation can produce characteristic oscillatory features in the gamma-ray spectrum within the mass range $m_a \sim 10^{-9}$–10^{-7} eV. No significant deviation from the standard astrophysical model is observed, allowing us to place constraints on the ALP parameter space. The resulting limits probe a region complementary to existing constraints from other astrophysical observations.

Keywords: axion-like particles; gamma rays; ALP-photon oscillation; M31

1. Introduction

ALPs [1–6] are light pseudoscalar bosons predicted in many extensions of the Standard Model. Owing to the ALP-photon coupling, photons can oscillate into ALPs in external magnetic fields during propagation. Such oscillations may leave observable imprints on high-energy gamma-ray spectra, including spectral irregularities, modulations, and deviations from smooth intrinsic shapes. For this reason, gamma-ray observations of astrophysical sources embedded in structured magnetic environments provide an important avenue for probing the ALP parameter space [7–24].

Existing constraints on the ALP-photon oscillation span a wide range of masses and observational approaches. At large masses, helioscope searches and stellar-evolution arguments already provide benchmark bounds at the level of $g_{a\gamma} \lesssim 6.6 \times 10^{-11}\,\mathrm{GeV}^{-1}$, as demonstrated by the CAST solar-axion search [25] and by analyses of Galactic globular clusters [26]. In the ultralight regime, the non-detection of a coincident γ-ray signal from SN1987A yields a much stronger constraint [27,28], $g_{a\gamma} \lesssim 5.3 \times 10^{-12}\,\mathrm{GeV}^{-1}$ for $m_a \lesssim 4.4 \times 10^{-10}$ eV. In the X-ray band, Chandra grating spectroscopy of NGC 1275 [29] and H1821+643 [30] constrains the coupling down to the level of a few $10^{-13}\,\mathrm{GeV}^{-1}$ for $m_a \lesssim 10^{-12}$ eV. In the γ-ray band, Fermi-LAT observations of NGC 1275 exclude $g_{a\gamma} \gtrsim 5 \times 10^{-12}\,\mathrm{GeV}^{-1}$ for $0.5 \lesssim m_a \lesssim 5$ neV [31], while MAGIC observations [32] of the Perseus cluster further probe the $m_a \sim$ few $\times$ 10–100 neV region with sensitivity at the level of $g_{a\gamma} \sim$ few $\times\, 10^{-12}\,\mathrm{GeV}^{-1}$.

These studies demonstrate that spectral-irregularity searches in magnetized astrophysical environments provide a powerful probe of ALPs. Most previous studies have extensively focused on distant blazars [8,33–38]. However, those analyses are often affected by the large uncertainty associated with cosmological propagation and the complex

Check for updates

Academic Editor: Ralf Hofmann

Received: 16 April 2026
Revised: 16 May 2026
Accepted: 18 May 2026
Published: 20 May 2026

Copyright: © 2026 by the author. Licensee MDPI, Basel, Switzerland. This article is an open access article distributed under the terms and conditions of the Creative Commons Attribution (CC BY) license.

environments of active galactic nuclei. In contrast, M31 offers a comparatively cleaner propagation environment for ALP studies, particularly because the uncertainties associated with cosmological propagation, EBL attenuation, and AGN jet physics are greatly reduced. Moreover, M31 has already been firmly detected in the GeV band by Fermi-LAT [39], providing a measured gamma-ray spectrum on which such effects can be tested. Therefore, M31 is not merely another extragalactic source for ALP searches. Instead, it serves as a benchmark object for testing the ALP-photon oscillation scenario in a nearby spiral-galaxy environment. This environment is distinct from those of Galactic sources and high-redshift blazars.

Recently, M31 has been characterized in increasing detail from the GeV band to radio polarization observations. A template-independent reconstruction of about 12 years of Fermi-LAT data suggested that the γ-ray emission of M31 contains a bulge-like component. Its angular extension is about 0.3–0.4°. A second component may also be present, extending to at least 1° [40]. A subsequent analysis based on ∼14 years of Fermi-LAT data [41] reaches a different conclusion. It argued that the central high-energy emission can be described by two point-like sources. One is consistent with the nucleus of M31, while the other is located about 0.4° to the south-east. This suggests that the detailed morphology of the source is still under active debate.

Meanwhile, radio polarization studies have continued to refine the magnetic environment of M31, which is particularly important for ALP-photon oscillations. The central region of M31 appears magnetically distinct from the outer disk: the spiral magnetic field in the inner ∼0.5 kpc points outward, opposite to that in the outer disk, with a pitch angle of about 33° [42]. In the prominent 7–12 kpc emission torus, recent measurements found average magnetic-field strengths of (6.3 ± 0.2) μG for the total field, (5.4 ± 0.2) μG for the isotropic turbulent component, and (3.2 ± 0.3) μG for the ordered field in the sky plane, while the axisymmetric regular field remains nearly constant at (2.0 ± 0.5) μG [43]. Very recent Fourier-mode analyses further confirm that the large-scale field of M31 is dominated by an axisymmetric spiral component over the radial range 6–14 kpc, with additional higher-order modes superposed on it [44].

These observational results make M31 a well-motivated target for ALP searches. It is close enough that the degeneracy related to cosmological propagation and extragalactic background light attenuation is greatly reduced. It still provides a well-resolved multi-zone magnetic environment, including the central region, the disk/ring region, and possible reconversion in the Galactic magnetic field. This makes it possible to test ALP-photon oscillations against the measured γ-ray spectrum.

This paper is organized as follows. In Section 2, we introduce the ALP-photon oscillation effect. In Section 3, we describe the astrophysical environment model for the VHE γ-ray photons propagating from M31 to the Earth. In Section 4, we describe the process of fitting the gamma-ray spectra and the statistical method. Our numerical results are presented in Section 5. In Section 6, we comment on our results and conclude.

2. ALP-Photon Oscillation

The interaction between axion-like particles (ALPs) and photons is described by the effective Lagrangian

$$\mathcal{L}_{a\gamma} = -\frac{1}{4} g_{a\gamma} a F_{\mu\nu} \tilde{F}^{\mu\nu} = g_{a\gamma} a \mathbf{E} \cdot \mathbf{B}, \quad (1)$$

where $g_{a\gamma}$ is the ALP-photon coupling constant and a denotes the ALP field. $\mathbf{E}$ and $\mathbf{B}$ denote the electric and magnetic fields, respectively. As photons propagate through astrophysical magnetic fields, they can oscillate into ALPs, leading to energy-dependent modulations in the observed spectrum.

The propagation of the ALP-photon system can be formulated by a Schrödinger-like equation,

$$i\frac{d}{dz}\Psi(z) = \mathcal{M}\,\Psi(z), \tag{2}$$

where $\Psi \equiv (A_\perp, A_\parallel, a)^T$ represents the two photon polarization states and the ALP component. The mixing matrix $\mathcal{M}$ includes the effects of the ALP mass, photon dispersion in the medium, and ALP-photon coupling. In particular, the off-diagonal term $\Delta_{a\gamma} = g_{a\gamma}B_T/2$ characterizes the mixing strength in the presence of a transverse magnetic field B_T, while the diagonal term $\Delta_a = -m_a^2/(2E)$ depends on the ALP mass m_a. Photon attenuation during propagation is modeled by including an imaginary absorption term in the evolution matrix.

The propagation path is divided into multiple domains, within each of which the magnetic field is assumed to be homogeneous. The total transfer matrix is obtained by multiplying the transfer matrices of all domains. Using the density matrix formalism, the photon survival probability can be written as

$$P_{\gamma\gamma} = \mathrm{Tr}\Big[(\rho_{11} + \rho_{22})\,T\,\rho(0)\,T^\dagger\Big], \tag{3}$$

where the initial density matrix for an unpolarized photon beam is given by $\rho(0) = \mathrm{diag}(1/2, 1/2, 0)$. T is the transfer matrix. Here, ρ_{11} and ρ_{22} are the projection matrices onto the two photon polarization states. In the basis $\Psi = (A_\perp, A_\parallel, a)^T$, they are given by

$$\rho_{11} = \begin{pmatrix} 1 & 0 & 0 \\ 0 & 0 & 0 \\ 0 & 0 & 0 \end{pmatrix}, \qquad \rho_{22} = \begin{pmatrix} 0 & 0 & 0 \\ 0 & 1 & 0 \\ 0 & 0 & 0 \end{pmatrix}.$$

Thus, $\rho_{11} + \rho_{22}$ projects the final state onto the photon subspace, and the photon survival probability is obtained by summing over the two photon polarization states.

3. Astrophysical Environments of M31

Radio polarization studies indicate that the central region of M31 is magnetically distinct from the outer disk [42], while the ring region hosts a well-developed large-scale axisymmetric field [43,45]. These properties make M31 a particularly suitable target for ALP searches because ALP-photon conversion depends sensitively on the transverse magnetic-field strength, coherence length, field geometry, and plasma density. The central region and the ordered disk/ring field of M31 provide physically motivated magnetic environments where such conversions may occur. At the same time, the proximity of M31 reduces uncertainties from cosmological propagation and extragalactic background light absorption. Thus, M31 offers a cleaner and complementary system for testing spectral modulations induced by ALP-photon conversions in comparison with distant blazars.

In this study, we divide the propagation path from M31 to the Earth into four main regions: the central region of M31, the disk/ring region of M31, the short intergalactic path inside the Local Group, and the magnetic field of the Milky Way. The total transfer matrix is written as

$$T(E) = T_{\mathrm{MW}}(E)\,T_{\mathrm{LG}}(E)\,T_{\mathrm{M31,disk}}(E)\,T_{\mathrm{M31,cen}}(E). \tag{4}$$

In the present analysis, only the large-scale ordered magnetic-field component is included in the transfer matrix. The turbulent component is expected to possess a much shorter coherence length and mainly induces stochastic decoherence effects, which tend to average out after propagation across many domains. Therefore, the dominant contribution to the observable large-scale spectral modulations is expected to arise from the coherent regular field.

3.1. Central Region of M31

The innermost region is potentially one of the most efficient ALP-photon oscillation zones because the conversion probability increases with the strength of the transverse magnetic field. In the central region of M31, the magnetic field is expected to be stronger than in the outer disk, while the propagation scale remains sufficiently large for efficient mixing. Radio polarization studies indicate that the magnetic structure within $r \lesssim 0.5$ kpc is distinct from that of the outer disk, and the spiral magnetic field in the center appears to point outward with a pitch angle of about 33° [42]. The magnetic-field strength in the central kiloparsec is inferred to be at the level of several to several tens of μG, which is substantially larger than the ordered component in the outer ring. For this reason, the central region should be treated as an independent mixing zone.

In the baseline model, we approximate the central region by an effective homogeneous transverse magnetic field and a constant electron density,

$$B_{\perp,\mathrm{cen}}(r) = B_{\mathrm{cen},0}, \qquad n_{e,\mathrm{cen}}(r) = n_{e,\mathrm{cen},0}, \qquad 0 \le r \le R_{\mathrm{cen}}, \tag{5}$$

where R_{cen} is the size of the central mixing region, $B_{\mathrm{cen},0}$ is the effective ordered transverse magnetic field, and $n_{e,\mathrm{cen},0}$ is the thermal electron density. As a benchmark, we adopt

$$R_{\mathrm{cen}} \sim 1\ \mathrm{kpc}, \qquad B_{\mathrm{cen},0} \sim \mathcal{O}(5\text{–}10)\,\mu\mathrm{G}, \qquad n_{e,\mathrm{cen},0} \sim \mathcal{O}(10^{-1})\ \mathrm{cm}^{-3}. \tag{6}$$

Here, $B_{\mathrm{cen},0}$ should be interpreted as an effective coherent ordered magnetic-field component relevant for ALP-photon mixing, rather than the total magnetic-field strength inferred from radio observations, which also includes turbulent and isotropic components. The adopted values are motivated by existing radio and Faraday-rotation studies of the large-scale magnetic environment of M31 [42,43,45].

Since the present analysis is mainly focused on the GeV band, internal $\gamma\gamma$ absorption in the central region is neglected in the baseline setup. If the analysis is extended to $E \gtrsim 100$ GeV, one may include an additional optical-depth term $\tau_{\mathrm{cen}}(E)$ to describe the absorption caused by stellar and infrared radiation fields in the bulge [46].

3.2. Disk and Ring Region of M31

Outside the central kiloparsec, the dominant magnetic environment is the disk/ring region of M31. Multi-wavelength radio polarization observations show that the regular magnetic field in the radial range 8–14 kpc is close to an axisymmetric spiral configuration, with a pitch angle in the range [45]

$$p_{\mathrm{M31}} \simeq -19^{\circ}\ \text{to}\ -8^{\circ}. \tag{7}$$

In this study, B_{tot}, B_{ord} and B_{reg} represent the total magnetic field strength inferred from the synchrotron intensity, the component with a coherent orientation in the plane of the sky and the large-scale axisymmetric spiral component, respectively. More recent studies [42,43,45] of the 8–12 kpc emission torus find average magnetic-field strengths of about

$$B_{\mathrm{tot}} \simeq (6.3 \pm 0.2)\,\mu\mathrm{G}, \qquad B_{\mathrm{ord}} \simeq (3.2 \pm 0.3)\,\mu\mathrm{G}, \qquad B_{\mathrm{reg}} \simeq (2.0 \pm 0.5)\,\mu\mathrm{G}, \tag{8}$$

indicating that M31 possesses one of the best-organized large-scale magnetic fields among nearby spiral galaxies [43].

Motivated by these observations, we model the disk/ring region with an exponentially declining transverse magnetic field,

$$B_{\perp,\mathrm{disk}}(r) = B_{\mathrm{disk},0}\,\exp\left[-\frac{r-r_0}{r_B}\right], \tag{9}$$

and an electron-density profile

$$n_{e,\mathrm{disk}}(r) = n_{e,\mathrm{disk},0}\,\exp\left[-\frac{r-r_0}{r_n}\right]. \tag{10}$$

Here r_0 is a reference radius, which we choose near the inner edge of the ring region, typically

$$r_0 \simeq 8\ \mathrm{kpc}. \tag{11}$$

In the benchmark model, according to Ref. [45], we adopt

$$B_{\mathrm{disk},0} \sim 3\ \mu\mathrm{G}, \qquad n_{e,\mathrm{disk},0} \sim 3\times 10^{-2}\ \mathrm{cm}^{-3}. \tag{12}$$

For GeV photons, the absorption due to starlight and dust-reprocessed infrared photons in the disk/ring region is expected to be weak and is therefore neglected in the baseline analysis. If TeV data or upper limits are included, this contribution can be described by an energy-dependent optical depth $\tau_{\mathrm{disk}}(E)$ [46].

Considering the magnetic-field structure and parameter configuration described above, we obtain the M31 magnetic-field distribution shown in Figure 1. In this figure, the colored arrows indicate the magnetic-field directions, while their colors schematically represent the relative magnetic-field strength: yellow and green denote stronger fields, whereas blue and purple denote weaker fields. The red and orange curves mark the ring and ring region. The gray regions indicate the central bulge and disk components. The cyan and green contours outline the adopted schematic disk and halo magnetic-field regions, respectively.

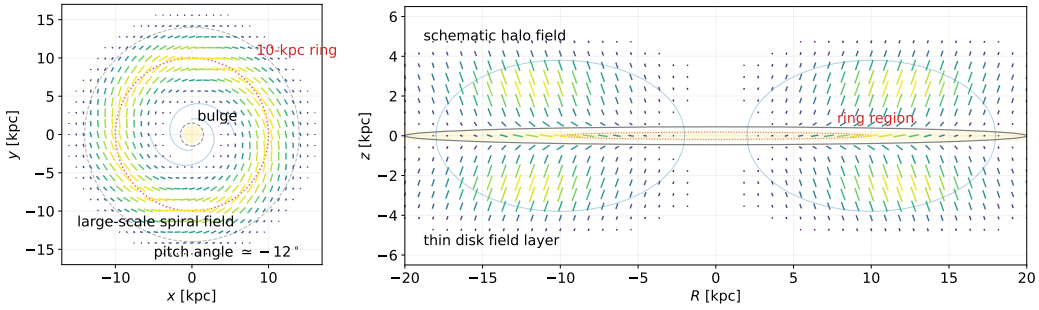


Figure 1. Schematic illustration of the magnetic environments of M31 relevant for ALP-photon propagation. The (**left**) panel shows a face-on view of the large-scale disk magnetic field, approximated by an axisymmetric spiral pattern with pitch angle $p_{\mathrm{M31}} \simeq -12^\circ$, together with the central bulge and the prominent ~ 10 kpc ring. The (**right**) panel shows an edge-on view of the effective M31 magnetic configuration, including the thin disk field layer and a schematic halo component.

3.3. Local Group Path

After escaping from M31, the ALP-photon beam propagates through the short intergalactic path between M31 and the Milky Way. This part of the propagation is qualitatively different from the case of distant blazars. The distance to M31 [41] is only about

$$D_{\mathrm{M31}} \simeq 750\text{–}780\ \mathrm{kpc}, \tag{13}$$

which is far too short for extragalactic background light (EBL) attenuation to play a major role in the GeV band [47]. Likewise, the magnetic field in the Local Group medium is poorly constrained and is expected to be much weaker than the μG-level fields in M31 and in the Milky Way [48]. Therefore, it is unlikely to produce a robust ALP-photon conversion signal in the baseline model. We neglect both EBL attenuation and ALP-photon mixing in this region, and approximate the corresponding transfer matrix by

$$T_{\rm LG}(E) \simeq \mathbb{I}, \tag{14}$$

where $\mathbb{I}$ is the identity matrix. This is one of the main advantages of M31 as an ALP target: compared with distant AGN, the degeneracy associated with cosmological propagation is greatly reduced.

The baseline propagation model adopted in this work is intended to represent a physically motivated and conservative description of the M31 environment, rather than an extreme configuration optimized for ALP-photon conversion. Several of the adopted parameters, particularly the electron density in the central region, tend to suppress the mixing effect through plasma contributions.

3.4. Milky Way Magnetic Field

Finally, the beam enters the Milky Way, where ALPs can reconvert into photons in the Galactic magnetic field. This contribution is expected to be one of the most robust parts of the propagation model, because it is independent of the uncertain internal morphology of M31. Following previous ALP studies [36,49], we describe the regular Galactic magnetic field with a standard large-scale model, which is the Jansson–Farrar model [50].

4. Method

The observed gamma-ray spectrum is then obtained by folding the intrinsic spectrum with the survival probability,

$$\frac{dN}{dE} = P_{\gamma\gamma}(E; m_a, g_{a\gamma}) \times \left(\frac{dN}{dE}\right)_{\rm int}. \tag{15}$$

We model the smooth intrinsic spectrum of M31 with a log-parabola (LP) form,

$$\left(\frac{dN}{dE}\right)_{\rm int} = N_0 \left(\frac{E}{E_b}\right)^{-[\alpha+\beta\log(E/E_b)]}. \tag{16}$$

Here, N_0 is the normalization, E_b is the scale energy, α is the spectral index at E_b, and β describes the spectral curvature.

To compare with observational data, we construct a chi-square function

$$\chi^2 = \sum_i \frac{\left[\Phi_i^{\rm model} - \Phi_i^{\rm obs}\right]^2}{\sigma_i^2}, \tag{17}$$

where $\Phi_i^{\rm obs}$ and σ_i are the measured flux and its uncertainty in the i-th energy bin of the SED, and $\Phi_i^{\rm model}$ is the predicted flux including ALP-photon oscillation. For each parameter point $(m_a, g_{a\gamma})$, the intrinsic spectral parameters are re-fitted to minimize χ^2.

We define the test statistic as

$$TS(m_a, g_{a\gamma}) = \chi^2_{\rm ALP} - \chi^2_{\rm null}, \tag{18}$$

where $\chi^2_{\rm null}$ corresponds to the best-fit result without ALPs, and $\chi^2_{\rm ALP}$ is obtained including the mixing effect. With this definition, negative values are possible in principle and would indicate that a given ALP parameter point improves the fit relative to the null model. Because the spectral distortions induced by ALP-photon oscillations are highly non-linear, the distribution of the test statistic does not follow a simple χ^2 distribution. Therefore, we adopt the CL$_s$ method [51–53] to evaluate the statistical significance.

For each parameter point, we generate Monte Carlo realizations of the data under both the signal-plus-background and background-only hypotheses. The flux in each energy bin is fluctuated according to a Gaussian distribution based on the expected value and experimental uncertainty. From these samples, we construct the distributions of the test statistic and compute

$$CL_s = \frac{CL_{s+b}}{CL_b}, \tag{19}$$

where CL_{s+b} denotes the probability of obtaining a test statistic larger than the observed value under the signal-plus-background hypothesis, while CL_b denotes the corresponding probability under the background-only hypothesis. A parameter point is excluded if $CL_s < 0.05$.

In the present scan, no ALP parameter point provides a statistically significant improvement over the null model. The map shown below is therefore used as an exclusion-oriented fit-degradation map rather than as a signal-significance map. The Fermi-LAT irregularity-search statistic is closely related in spirit, but our purpose here is to set exclusion limits for fixed ALP parameter points using the published M31 SED. The CL$_s$ method is suitable for this purpose and has also been used in previous ALP constraint studies.

Finally, we scan the ALP parameter space in $(m_a, g_{a\gamma})$ and derive the exclusion limits based on the observed M31 gamma-ray spectrum.

5. Results

Figure 2 shows the energy dependence of the photon survival probability $P_{\gamma\gamma}$ for M31 in the presence of ALP-photon oscillations. The results demonstrate that the M31 magnetic environment induces characteristic oscillatory structures in $P_{\gamma\gamma}$, whose energy scale and amplitude are controlled by the ALP mass and coupling, respectively.

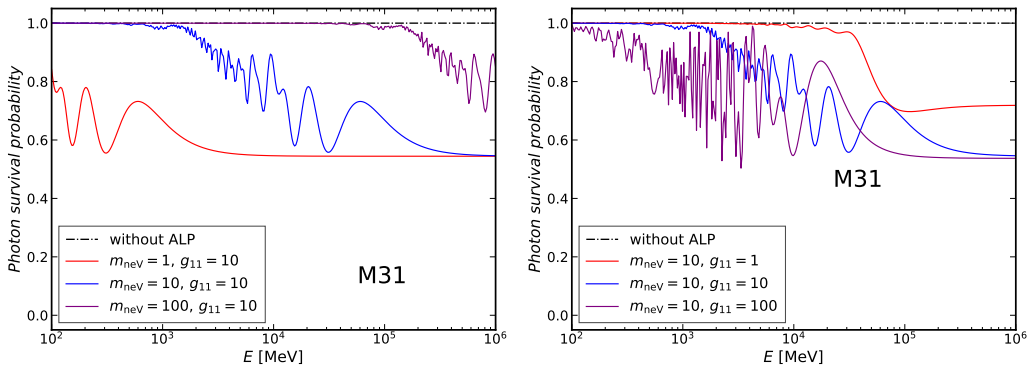


Figure 2. Energy dependence of the photon survival probability $P_{\gamma\gamma}$ for M31 in the presence of ALP-photon oscillations. The black dash-dotted curve corresponds to the no-ALP case. (**Left**): $g_{11} = 10$ is fixed and the ALP mass is varied, with $m_{\rm neV} = 1,\ 10,\ 100$. (**Right**): $m_{\rm neV} = 10$ is fixed and the coupling is varied, with $g_{11} = 1,\ 10,\ 100$. Here $m_{\rm neV} \equiv m_a/(1\ {\rm neV})$ and $g_{11} \equiv g_{a\gamma}/(10^{-11}\ {\rm GeV}^{-1})$. The figure demonstrates that the M31 magnetic environment can induce characteristic oscillatory structures in $P_{\gamma\gamma}$, whose energy scale and amplitude are controlled by the ALP mass and coupling.

A comparison between the observed M31 spectral energy distribution (SED) and the ALP-photon modulated spectra is presented in Figure 3. The black dash-dotted curve denotes the best-fit log-parabola spectrum without ALPs, and the gray shaded region shows the corresponding 68% confidence band. For each ALP parameter set, the intrinsic spectral parameters are re-fitted after applying the photon survival probability. The black data points represent Fermi-LAT measurements, with horizontal error bars indicating the energy-bin widths and arrows indicating upper limits. The left panel fixes $g_{11} = 10$ and varies $m_{\rm neV} = 1,\ 10,\ 100$, while the right panel fixes $m_{\rm neV} = 10$ and varies $g_{11} = 1,\ 10,\ 100$. The figure illustrates how different ALP parameter choices can produce different energy-dependent spectral modulations. No statistically significant deviation from the smooth spectral model is found, and the resulting constraints should be interpreted in view of the limited energy binning of the available SED.

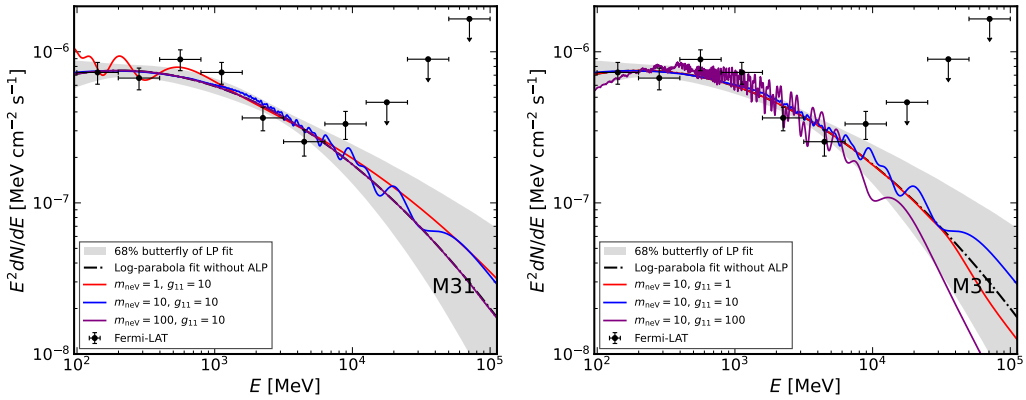


Figure 3. Comparison between the observed M31 spectral energy distribution and the best-fit spectral models. The black dash-dotted curve denotes the best-fit log-parabola spectrum without ALPs, and the gray shaded region shows its 68% confidence band. The colored curves show the corresponding ALP-modified spectra after re-fitting the intrinsic spectral parameters. The black points represent the Fermi-LAT measurements, with horizontal error bars indicating the energy-bin widths and arrows indicating upper limits. (**Left**) panel: the coupling is fixed at $g_{11} = 10$, while the ALP mass is varied as $m_{\rm neV} = 1,\ 10,\ 100$. (**Right**) panel: the ALP mass is fixed at $m_{\rm neV} = 10$, while the coupling is varied as $g_{11} = 1,\ 10,\ 100$. Here $m_{\rm neV} \equiv m_a/(1\ \text{neV})$ and $g_{11} \equiv g_{a\gamma}/(10^{-11}\ \text{GeV}^{-1})$.

The left panel of Figure 4 shows the relative fit-degradation map in the $(m_a,\ g_{a\gamma})$ plane obtained from our ALP fit. The orange contours enclose the excluded regions. We find that the excluded regions mainly appear near $m_a \sim \mathcal{O}(10^{-8})$ eV and $g_{a\gamma} \sim \mathcal{O}(10^{-11})$ GeV^{-1}, where the ALP-induced spectral modulations are most pronounced in the Fermi-LAT energy range. The right panel of Figure 4 compares the excluded regions from this work (orange contours) with existing constraints from HAWC TeV blazars [54], GRB221009A [18], MAGIC observations of Mrk 421 [17], H.E.S.S. observations of PKS 2155−304 [55], and CAST [25]. Our results provide an independent and complementary test of ALP-photon oscillations in a nearby spiral-galaxy environment in the $m_a \sim 10^{-9}$–10^{-7} eV mass range.

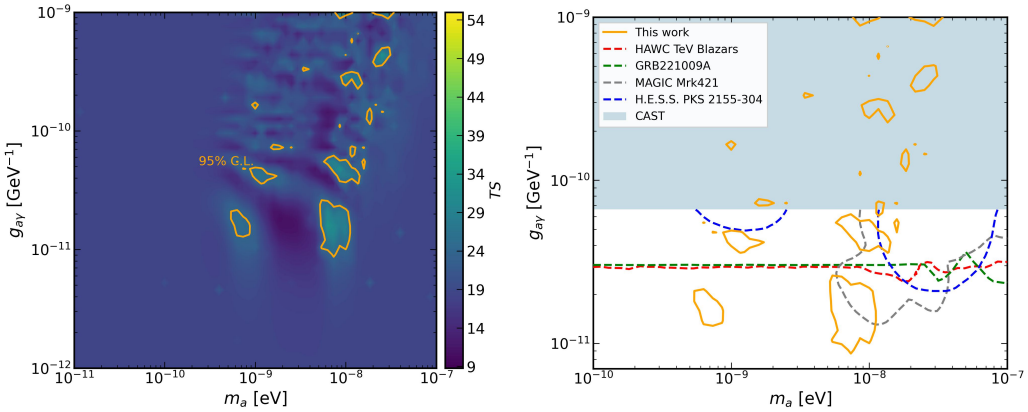


Figure 4. (**Left**): Relative fit-degradation map in the $(m_a, g_{a\gamma})$ plane. The orange contours denote the 95% C.L. exclusion contours obtained in this study. (**Right**): The same exclusion contours from this work (orange), compared with existing constraints from HAWC TeV blazars, GRB221009A, MAGIC observations of Mrk 421, H.E.S.S. observations of PKS 2155−304, and CAST.

6. Conclusions

In this work, we have investigated the impact of ALP-photon mixing on the gamma-ray spectrum of M31 and derived constraints on the ALP parameter space using the available observational data. By modeling the photon propagation in the M31 magnetic environment and incorporating the effects of ALP-photon oscillations, we quantified the resulting spectral modulations and compared them with the observed gamma-ray spectrum.

Our analysis shows that ALP-photon coupling can induce characteristic energy-dependent oscillatory features in the photon survival probability, which translate into distortions in the gamma-ray spectrum. These features depend sensitively on both the ALP mass m_a and the ALP-photon coupling $g_{a\gamma}$. In particular, the M31 magnetic field can generate observable signatures in the mass range $m_a \sim 10^{-9}$–10^{-7} eV, where the mixing effect becomes efficient.

By performing a spectral fit to the M31 data, we find that no statistically significant deviation from the standard astrophysical expectation is required. The absence of strong spectral irregularities allows us to place constraints on the ALP parameter space. The resulting limits probe a region that is complementary to those derived from other astrophysical observations, such as blazars and Galactic sources.

We also note that the exclusion contours are not continuous, but split into separated islands and bands. This pattern arises because ALP-photon oscillation modifies the spectrum in an energy-dependent and non-monotonic way, so that nearby parameter points can lead to markedly different spectral features.

The main sources of uncertainty in our analysis arise from the modeling of the magnetic field and the intrinsic gamma-ray spectrum of M31. Variations in these assumptions may affect the detailed shape of the constraints, although the overall sensitivity remains robust.

Future gamma-ray observations with improved statistics, broader energy coverage, and better energy resolution will significantly enhance the sensitivity to ALP-photon mixing effects. In particular, next-generation instruments are expected to probe smaller values of $g_{a\gamma}$ and test a wider range of ALP masses. Combined analyses including multiple sources and refined magnetic field models will further strengthen the constraints and improve our understanding of ALP phenomenology. The present analysis should be interpreted as a search for relatively broad ALP-induced spectral modulations rather than a fully optimized fine-binned irregularity search. A dedicated Fermi-LAT likelihood analysis with finer

energy binning and a careful treatment of energy dispersion would be required for a more sensitive search for narrow spectral features.

Overall, our analysis demonstrates that gamma-ray observations of M31 can provide an independent probe of ALP-photon mixing effects in the mass range $m_a \sim 10^{-9}$–10^{-7} eV. The absence of significant broad spectral modulations in the present data allows us to place constraints on the ALP-photon coupling, while future observations with improved statistics and energy resolution are expected to further tighten these bounds.

Funding: This research was funded by Xinjiang Natural Science Foundation, grant number 2025D01C287.

Data Availability Statement: No new observational data are generated in this study. The spectral data points used in this work are taken from the published results of [39].

Conflicts of Interest: The authors declare no conflicts of interest. The funders had no role in the design of the study; in the collection, analyses, or interpretation of data; in the writing of the manuscript; or in the decision to publish the results.

References

1. Arias-Aragón, F.; Quevillon, J.; Smith, C. Axion-like ALPs. *J. High Energy Phys.* **2023**, *2023*, 134. [CrossRef]
2. Marsh, M.C.D.; Russell, H.R.; Fabian, A.C.; McNamara, B.R.; Nulsen, P.; Reynolds, C.S. A new bound on axion-like particles. *J. Cosmol. Astropart. Phys.* **2017**, *2017*, 036. [CrossRef]
3. Bauer, M.; Heiles, M.; Neubert, M.; Thamm, A. Axion-like particles at future colliders. *Eur. Phys. J. C* **2019**, *79*, 74. [CrossRef]
4. Chadha-Day, F. Axion-like particle oscillations. *J. Cosmol. Astropart. Phys.* **2022**, *2022*, 013. [CrossRef]
5. Galanti, G. Axion-like particles and high energy astrophysics. *arXiv* **2019**, arXiv:1911.09372. [CrossRef]
6. Galanti, G. Axion-like particle effects on photon polarization in high-energy astrophysics. *Universe* **2024**, *10*, 312. [CrossRef]
7. Berenji, B.; Gaskins, J.; Meyer, M. Constraints on Axions and Axionlike Particles from Fermi Large Area Telescope Observations of Neutron Stars. *Phys. Rev. D* **2016**, *93*, 045019. [CrossRef]
8. Galanti, G.; Tavecchio, F.; Roncadelli, M.; Evoli, C. Blazar VHE spectral alterations induced by photon-ALP oscillations. *Mon. Not. R. Astron. Soc.* **2019**, *487*, 123–132. [CrossRef]
9. Galanti, G.; Roncadelli, M. Extragalactic photon-axion-like particle oscillations up to 1000 TeV. *J. High Energy Astrophys.* **2018**, *20*, 1–17. [CrossRef]
10. Zhang, C.; Liang, Y.-F.; Li, S.; Liao, N.-H.; Feng, L.; Yuan, Q.; Fan, Y.-Z.; Ren, Z.-Z. New bounds on axionlike particles from the Fermi Large Area Telescope observation of PKS 2155-304. *Phys. Rev. D* **2018**, *97*, 063009. [CrossRef]
11. Liang, Y.-F.; Zhang, C.; Xia, Z.-Q.; Feng, L.; Yuan, Q.; Fan, Y.-Z. Constraints on axion-like particle properties with TeV gamma-ray observations of Galactic sources. *J. Cosmol. Astropart. Phys.* **2019**, *2019*, 042. [CrossRef]
12. Xia, Z.-Q.; Zhang, C.; Liang, Y.-F.; Feng, L.; Yuan, Q.; Fan, Y.-Z.; Wu, J. Searching for spectral oscillations due to photon-axionlike particle conversion using the Fermi-LAT observations of bright supernova remnants. *Phys. Rev. D* **2018**, *97*, 063003. [CrossRef]
13. Bi, X.-J.; Gao, Y.; Guo, J.; Houston, N.; Li, T.; Xu, F.; Zhang, X. Axion and dark photon limits from Crab Nebula high energy gamma-rays. *Phys. Rev. D* **2021**, *103*, 043018. [CrossRef]
14. Guo, J.; Li, H.-J.; Bi, X.-J.; Lin, S.-J.; Yin, P.-F. Implications of axion-like particles from the Fermi-LAT and H.E.S.S. observations of PG 1553+113 and PKS 2155-304. *Chin. Phys. C* **2021**, *45*, 025105.
15. Li, H.-J.; Guo, J.-G.; Bi, X.-J.; Lin, S.-J.; Yin, P.-F. Limits on axion-like particles from Mrk 421 with 4.5-year period observations by ARGO-YBJ and Fermi-LAT. *Phys. Rev. D* **2021**, *103*, 083003.
16. Liang, Y.-F.; Zhang, X.-F.; Cheng, J.-G.; Zeng, H.-D.; Fan, Y.-Z.; Liang, E.-W. Effect of axion-like particles on the spectrum of the extragalactic gamma-ray background. *J. Cosmol. Astropart. Phys.* **2021**, *2021*, 030.
17. Gao, L.-Q.; Bi, X.-J.; Guo, J.-G.; Lin, W.; Yin, P.-F. Constraints on axionlike particles from observations of Mrk 421 using the CLs method. *Phys. Rev. D* **2024**, *109*, 063003.
18. Gao, L.-Q.; Bi, X.-J.; Li, J.; Yao, R.-M.; Yin, P.-F. Constraints on axion-like particles from the observation of GRB 221009A by LHAASO. *J. Cosmol. Astropart. Phys.* **2024**, *2024*, 026. [CrossRef]
19. Majumdar, J.; Calore, F.; Horns, D. Search for gamma-ray spectral modulations in Galactic pulsars. *J. Cosmol. Astropart. Phys.* **2018**, *2018*, 048. [CrossRef]
20. Xia, Z.-Q.; Liang, Y.-F.; Feng, L.; Yuan, Q.; Fan, Y.-Z.; Wu, J. Searching for the possible signal of the photon-axionlike particle oscillation in the combined GeV and TeV spectra of supernova remnants. *Phys. Rev. D* **2019**, *100*, 123004.
21. Eckner, C.; Calore, F. First constraints on axionlike particles from Galactic sub-PeV gamma rays. *Phys. Rev. D* **2022**, *106*, 083020. [CrossRef]

22. Galanti, G.; Roncadelli, M.; Tavecchio, F.; Costa, E. ALP induced polarization effects on photons from galaxy clusters. *Phys. Rev. D* **2023**, *107*, 103007. [CrossRef]
23. Dessert, C.; Dunsky, D.; Safdi, B.R. Upper limit on the axion-photon coupling from magnetic white dwarf polarization. *Phys. Rev. D* **2022**, *105*, 103034.
24. Safdi, B.R.; Sun, Z.; Chen, A.Y. Detecting Axion Dark Matter with Radio Lines from Neutron Star Populations. *Phys. Rev. D* **2019**, *99*, 123021. [CrossRef]
25. Anastassopoulos, V. et al. [CAST Collaboration]. New CAST limit on the axion–photon interaction. *Nat. Phys.* **2017**, *13*, 584–590. [CrossRef]
26. Ayala, A.; Domínguez, I.; Giannotti, M.; Mirizzi, A.; Straniero, O. Revisiting the bound on axion-photon coupling from globular clusters. *Phys. Rev. Lett.* **2014**, *113*, 191302. [CrossRef]
27. Payez, A.; Evoli, C.; Fischer, T.; Giannotti, M.; Mirizzi, A.; Ringwald, A. Revisiting the SN1987A gamma-ray limit on ultralight axion-like particles. *J. Cosmol. Astropart. Phys.* **2015**, *2015*, 006. [CrossRef]
28. Hoof, S.; Schulz, L. Updated constraints on axion-like particles from temporal information in supernova SN1987A gamma-ray data. *J. Cosmol. Astropart. Phys.* **2023**, *2023*, 054. [CrossRef]
29. Reynolds, C.S.; Marsh, M.C.D.; Russell, H.R.; Fabian, A.C.; Smith, R.N.; Tombesi, F.; Veilleux, S. Astrophysical limits on very light axion-like particles from Chandra grating spectroscopy of NGC 1275. *Astrophys. J.* **2020**, *890*, 59. [CrossRef]
30. Sisk-Reynés, J.; Matthews, J.H.; Reynolds, C.S.; Russell, H.R.; Smith, R.N.; Marsh, M.C.D. New constraints on light axion-like particles using Chandra transmission grating spectroscopy of the powerful cluster-hosted quasar H1821+643. *Mon. Not. R. Astron. Soc.* **2022**, *510*, 1264–1286. [CrossRef]
31. Ajello, M. et al. [Fermi-LAT Collaboration]. Search for spectral irregularities due to photon-axionlike-particle oscillations with the Fermi Large Area Telescope. *Phys. Rev. Lett.* **2016**, *116*, 161101. [CrossRef]
32. Abe, H. et al. [MAGIC Collaboration]. Constraints on axion-like particles with the Perseus Galaxy Cluster with MAGIC. *Phys. Dark Universe* **2024**, *44*, 101425. [CrossRef]
33. Galanti, G.; Roncadelli, M.; Tavecchio, F. ALP-induced polarization effects on photons from blazars. *Phys. Rev. D* **2023**, *108*, 083017. [CrossRef]
34. Li, H.-J. Probing photon-ALP oscillations from the flat spectrum radio quasar 4C+ 21.35. *Phys. Lett. B* **2022**, *829*, 137047. [CrossRef]
35. Pant, B.P. Probing photon-ALP oscillations from the MAGIC observations of FSRQ QSO B 1420+ 326. *Phys. Rev. D* **2024**, *109*, 023011. [CrossRef]
36. Li, J.; Bi, X.-J.; Gao, L.-Q.; Yin, P.-F. Exploring axion-like particle from observation of FSRQ Ton 599 by Fermi-LAT. *Chin. Phys. C* **2025**, *49*, 105107. [CrossRef]
37. Tavecchio, F.; Roncadelli, M.; Galanti, G.; Bonnoli, G. Evidence for an axion-like particle from PKS 1222+216? *Phys. Rev. D* **2012**, *86*, 085036. [CrossRef]
38. Yu, Q. Searching for Signals of Photon-ALP Mixing Effects with Gamma-Ray Spectra of AGNs. Ph.D. Dissertation, University of Hamburg, Hamburg, Germany, 2023.
39. Ackermann, M. et al. [Fermi-LAT Collaboration]. Observations of M31 and M33 with the Fermi Large Area Telescope: A Galactic Center Excess in Andromeda? *Astrophys. J.* **2017**, *836*, 208. [CrossRef]
40. Armand, C.; Calore, F. Gamma-ray image reconstruction of the Andromeda galaxy. *Phys. Rev. D* **2021**, *103*, 083023. [CrossRef]
41. Xing, Y.; Wang, Z.; Zheng, D.; Li, J. On the Gamma-Ray Emission of the Andromeda Galaxy M31. *Astrophys. J. Lett.* **2023**, *945*, L22. [CrossRef]
42. Gießübel, R.; Beck, R. The magnetic field structure of the central region in M31. *Astron. Astrophys.* **2014**, *571*, A61. [CrossRef]
43. Beck, R.; Berkhuijsen, E.M. Magnetic fields and cosmic rays in M31. II. Strength and distribution of the magnetic field components. *Astron. Astrophys.* **2025**, *700*, A198. [CrossRef]
44. Paul, I.; Kashyap, R.V.; Ghosh, T.; Beck, R.; Chamandy, L.; Sinha, S.; Shukurov, A. The fine structure of the mean magnetic field in M31. *Mon. Not. R. Astron. Soc.* **2026**, *545*, staf2041. [CrossRef]
45. Fletcher, A.; Berkhuijsen, E.M.; Beck, R.; Shukurov, A. The magnetic field of M31 from multi-wavelength radio polarization observations. *Astron. Astrophys.* **2004**, *414*, 53–67. [CrossRef]
46. Moskalenko, I.V.; Porter, T.A.; Strong, A.W. Attenuation of Very High Energy Gamma Rays by the Milky Way Interstellar Radiation Field. *Astrophys. J. Lett.* **2006**, *640*, L155–L158. [CrossRef]
47. Dominguez, A.; Primack, J.R.; Rosario, D.J.; Prada, F.; Gilmore, R.C.; Faber, S.M.; Koo, D.C.; Somerville, R.S.; Pérez-Torres, M.A.; Pérez-González, P.; et al. Extragalactic background light inferred from AEGIS galaxy-SED-type fractions. *Mon. Not. R. Astron. Soc.* **2011**, *410*, 2556–2578. [CrossRef]
48. Durrer, R.; Neronov, A. Cosmological Magnetic Fields: Their Generation, Evolution and Observation. *Astron. Astrophys. Rev.* **2013**, *21*, 62. [CrossRef]
49. Li, J.; Bi, X.-J.; Gao, L.-Q.; Huang, X.; Yao, R.-M.; Yin, P.-F. Constraints on axion-like particles from the observation of Galactic sources by the LHAASO. *Chin. Phys. C* **2024**, *48*, 065107. [CrossRef]

50. Jansson, R.; Farrar, G.R. A new model of the Galactic magnetic field. *Astrophys. J.* **2012**, *757*, 14. [CrossRef]
51. Junk, T. Confidence Level Computation for Combining Searches with Small Statistics. *Nucl. Instrum. Methods Phys. Res. Sect. A* **1999**, *434*, 435–443. [CrossRef]
52. Read, A.L. Presentation of search results: The CL_s technique. *J. Phys. G Nucl. Part. Phys.* **2002**, *28*, 2693–2704. [CrossRef]
53. Lista, L. Practical Statistics for Particle Physicists. In Proceedings of the 2016 European School of High-Energy Physics, Skeikampen, Norway, 15–28 June 2016; pp. 213–258.
54. Jacobsen, S.; Linden, T.; Freese, K. Constraining axion-like particles with HAWC observations of TeV blazars. *J. Cosmol. Astropart. Phys.* **2023**, *2023*, 009. [CrossRef]
55. Abramowski, A. et al. [H.E.S.S. Collaboration]. Constraints on axionlike particles with H.E.S.S. from the irregularity of the PKS 2155−304 energy spectrum. *Phys. Rev. D* **2013**, *88*, 102003. [CrossRef]

Disclaimer/Publisher's Note: The statements, opinions and data contained in all publications are solely those of the individual author(s) and contributor(s) and not of MDPI and/or the editor(s). MDPI and/or the editor(s) disclaim responsibility for any injury to people or property resulting from any ideas, methods, instructions or products referred to in the content.